

Formation of mixed-layer sulfide-hydroxide minerals from the Tochilinite-Valleriite group during experimental serpentinization of olivine

THOMAS M. MCCOLLOM^{1,*}, TORI HOEHLER², DAVID A. FIKE³, JENNIFER L. HOUGHTON³,
AARON BELL⁴, FRIEDER KLEIN⁵, BRUCE MOSKOWITZ⁶, AND PETER SOLHEID⁶

¹Laboratory for Atmospheric and Space Physics, University of Colorado, Boulder, Colorado 80309, U.S.A.

²NASA Ames Research Center, Moffett Field, California 94035 U.S.A.

³Department of Earth and Planetary Sciences, Washington University in St. Louis, St. Louis, Missouri 63130, U.S.A.

⁴Department of Geological Sciences, University of Colorado, Boulder, Colorado 80309, U.S.A.

⁵Department of Marine Chemistry and Geochemistry, Woods Hole Oceanographic Institution, Woods Hole, Massachusetts 02543, U.S.A.

⁶Department of Earth and Environmental Sciences and Institute for Rock Magnetism, University of Minnesota, Minneapolis, Minnesota 55455, U.S.A.

ABSTRACT

We report the formation of minerals from the tochilinite-valleriite group (TVG) during laboratory serpentinization experiments conducted at 300 and 328 °C. Minerals in the TVG are composed of a mixture of sulfide and hydroxide layers that can contain variable proportions of Fe, Mg, Cu, Ni, and other cations in both layers. Members of this group have been observed as accessory minerals in several serpentinites, and have also been observed in association with serpentine minerals in meteorites. To our knowledge, however, TVG minerals have not previously been identified as reaction products during laboratory simulation of serpentinization. The serpentinization experiments reacted olivine with artificial seawater containing ³⁴S-labeled sulfate, with a small amount of solid FeS also added to the 300 °C experiment. In both experiments, the predominant reaction products were chrysotile serpentine, brucite, and magnetite. At 300 °C, these major products were accompanied by trace amounts of the Ni-bearing TVG member haapalaite, Ni,Fe-sulfide (likely pentlandite), and anhydrite. At 328 °C, valleriite occurs rather than haapalaite and the accompanying Ni,Fe-sulfide is proportionally more enriched in Ni. Reduction of sulfate by H₂ produced during serpentinization evidently provided a source of reduced S that contributed to formation of the TVG minerals and Ni,Fe-sulfides. The results provide new constraints on the conditions that allow precipitation of tochilinite-valleriite group minerals in natural serpentinites.

Keywords: Tochilinite, valleriite, haapalaite, serpentinization, sulfate reduction

INTRODUCTION

Tochilinite and valleriite are the most common representatives of a structurally related group of minerals that are composed of alternating sulfide and hydroxide layers (referred to herein as the tochilinite-valleriite group, or TVG; Organova et al. 1971; Makovicky and Hyde 1981; Zolensky 1987; Beard 2000). Minerals in this group have a nominal composition of 2(Fe,Cu,Ni) S·1.67(Mg,Fe)OH₂, although TVG minerals exhibit substantial variability in the relative abundances of Fe, Mg, Ni, and Cu and, in many instances, include additional components such as Al, Ca, Cr, and CO₃ (e.g., Huhma et al. 1973; Zolensky 1987; Beard 2000; Mücke 2017; Mikhlin et al. 2022a). Several compositional end-members within the group have been defined (e.g., Evans and Allmann 1968; Organova et al. 1971; Huhma et al. 1973), but the extent of solid solution among these end-members remains poorly understood.

Several studies have reported TVG minerals as accessory components of serpentinite (Chamberlain and Delabio 1965; Jambor 1969; Clark 1970; Organova et al. 1971; Harris and Vaughan 1972; Huhma et al. 1973; van de Vusse and Powell 1983; Matsubara and Kato 1992; Alt and Shanks 1998; Beard 2000; Beard and Hopkinson 2000; Dietze and Kontny 2011; Boschi et al. 2017; Mücke 2017; Mikhlin et al. 2022b; note that in some early studies TVG minerals were identified as “fibrous Fe sulfide”). In at least some

cases, TVG minerals are sufficiently abundant to be considered as rock-forming minerals or to be the predominant reservoir of S in serpentinite (e.g., Beard 2000). Tochilinite, the Fe-rich end-member of the group, is also a common secondary alteration component of carbonaceous chondrite meteorites, where in many cases it occurs in close association with the Fe-rich serpentine mineral cronstedtite (e.g., Zolensky 1987; Zolensky et al. 1993; Palmer and Lauretta 2011; Pignatelli et al. 2017).

Few experimental studies have investigated the circumstances under which TVG minerals precipitate in geologic environments, and these have primarily examined formation of tochilinite during alteration of native metal alloys relevant to meteorite parent bodies (e.g., Peng et al. 2007; Peng and Jing 2014; Vacher et al. 2019). To our knowledge, formation of TVG minerals has not previously been reported during experimental serpentinization of ultramafic rocks or their constituent minerals. As a consequence, current experimental data provide only very limited insight into the circumstances under which TVG minerals form in natural serpentinites.

Here, we report precipitation of the TVG minerals haapalaite and valleriite during experimental serpentinization of olivine following reaction with artificial seawater at 300 and 328 °C. The results provide insight into possible pathways for formation of TVG minerals in serpentinite. The experiments were part of a series designed to investigate the temperature dependence of sulfate reduction rates during serpentinization. The present communication focuses only on documentation of the occurrence of TVG minerals

* E-mail: mccollom@lasp.colorado.edu. Orcid 0000-0002-3596-5588

and the circumstances under which they form. Evaluation of sulfate reduction rates during this series of experiments will be the subject of a future communication.

METHODS

Two laboratory experiments were conducted by heating finely powdered olivine with artificial seawater at either 300 or 328 °C (designated SO4red300 and SO4red328, respectively). Both experiments were conducted at 35 MPa, with SO4red300 heated for 4001 h (167 days) and SO4red328 for 4028 h (168 days). The elevated pressure was used to nominally represent conditions during serpentinization of rocks within the oceanic crust, where most TVG mineral-bearing serpentinite is formed.

The artificial seawater solution was composed of 455 mmol kg⁻¹ NaCl, 31.5 mmol kg⁻¹ MgCl₂, 21.3 mmol kg⁻¹ MgSO₄, 9.7 mmol kg⁻¹ KCl, 9.2 mmol kg⁻¹ CaCl₂, and 2.3 mmol kg⁻¹ NaH¹³CO₃, and had a room-temperature pH (pH_{25°C}) of 8.5. Because the primary objective of the experiments was to examine sulfate reduction rates, the fluid also included 5.5 mmol kg⁻¹ Na₂SO₄ containing 90% ³⁴S to provide an isotopic label to track the fate of added sulfate. A small amount of FeS powder (500 ppmw) was also included in the SO4red300 experiment because previous studies have found that initiation of sulfate reduction is promoted by small amounts of reduced sulfur (e.g., Toland 1960; Zhang et al. 2008), presumably because the first step in the reduction involves formation of intermediate oxidation state compounds such as thiosulfate or native sulfur. No FeS was included in SO4red328. SO4red300 initially contained 14.0 g olivine, 7 mg FeS, and 38.1 g fluid, while SO4red328 contained 14.1 g olivine and 37.6 g fluid.

The experiments were conducted in a flexible-cell hydrothermal apparatus using a gold reaction cell with titanium fittings (Online Materials¹ Fig. S1; Seyfried et al. 1987). The reaction cell was contained within a stainless-steel pressure housing, with water used as the external pressurizing medium. The flexibility of the gold reaction cell allows the fluid to be sampled without loss of pressure, and eliminates the presence of a vapor headspace so that reactions are confined to the aqueous phase. The titanium fittings exposed to reactants during the experiments were heated in air for more than 24 h at 450 °C prior to use to form a relatively inert TiO₂ surface layer.

The experiments used olivine from San Carlos, Arizona, which has an approximate composition of Mg_{0.82}Fe_{0.18}SiO₄ (Fo₈₀; Table 1). The olivine powder was prepared from polished crystals >5 mm in diameter purchased from Excalibur Minerals (Charlottesville, Virginia), with separate batches of olivine powder prepared for each experiment. Only clear olivine crystals that were free of mineral inclusions or weathering products during inspection under a binocular microscope were selected for use in the experiments. The crystals were rinsed with deionized water and then crushed using a ceramic mortar and pestle, always avoiding the use of metal tools that might result in contamination of the reactants with particles of metal. Because

one of the primary objectives of the experiment was to rapidly generate H₂ to observe reduction of sulfate on a reasonable timescale, the olivine was sieved to obtain a fine powder (<53 µm) to promote rapid serpentinization (Online Materials¹ Figs. S2a and S2b). Fine-grained FeS powder (~100 mesh, <125 µm) was purchased from Alfa Aesar, and analysis of this synthetic material by X-ray diffraction (XRD) produced a pattern consistent with pyrrhotite. The abundance of sulfur in the prepared olivine as well as the isotopic composition of sulfur in the olivine and FeS were determined using methods described in the Online Materials¹.

The prepared olivine reactant was examined for impurities using scanning electron microscopy coupled with energy-dispersive X-ray spectroscopy (SEM/EDS). Extensive inspection of the olivine used in SO4red328 in backscattered electron mode to identify high-contrast minerals revealed only a single grain that contained S, which was a Cu-sulfide (Online Materials¹ Fig. S2d). Trace amounts of Fe- and Fe,Ti-oxides, spinel, and orthopyroxene, and a few clusters of Cu-oxide minerals were also observed sparsely scattered across the sample (Online Materials¹ Fig. S2c). No Cu-bearing phases were found in the olivine used in SO4red300. Other than olivine, no Ni-bearing minerals were identified during analysis of the reactants for either experiment.

At several intervals during the experiments, multiple fluid aliquots (0.3–1 g each) were obtained through the sample valve directly into gas-tight glass syringes. The aliquots were analyzed for the abundance of: (1) dissolved H₂; (2) total dissolved CO₂ [Σ CO₂ = CO_{2(aq)} + HCO₃⁻ + CO₃²⁻], CH₄, and C₂–C₆ hydrocarbons; (3) room-temperature pH (pH_{25°C}); (4) total dissolved sulfate (Σ SO₄) and H₂S [Σ H₂S = H₂S_(aq) + HS⁻]; (5) dissolved SiO₂; (6) major cations and, for a few samples; and (7) Cl. In one instance, the headspace of a sample obtained with a gas-tight syringe containing a small amount of phosphoric acid was injected into a benchtop gas chromatograph-mass spectrometer (GC-MS) to evaluate the isotopic composition of exsolved Σ H₂S. The isotopic composition of Σ SO₄ was also measured for the starting solution and for the fluid recovered after termination of SO4red328. Details of the analytical methods used to quantify aqueous species are provided as Online Materials¹.

At the termination of the experiments, the reacted solids were recovered and rinsed several times with ethanol in an effort to remove the remaining fluid. Various analytical methods were employed to characterize the solid products; details of the analytical methods are provided in the Online Materials¹ and briefly summarized here. The morphology of mineral products was evaluated with SEM/EDS using a Hitachi SU3500 scanning electron microscope equipped with an Oxford Instruments energy-dispersive X-ray spectrometer. Solids were examined both as grains mounted on Al stubs with carbon tape and as polished thin sections embedded in epoxy and coated with carbon, using an accelerating voltage of 15 kV. Analysis of the products by X-ray diffraction (XRD) was performed using a Terra instrument (Olympus, Inc.) with CuK α radiation. Electron microprobe analysis (EMPA) of polished thin sections was performed on a JEOL 8230 electron microprobe using a beam energy of 15 keV,

TABLE 1. Chemical compositions of minerals as determined by electron microprobe analysis

Oxide (wt%)	SC Olivine	SO4red300 Chrysotile (n = 9)	SO4red300 Brucite (n = 6)	SO4red300 Haapalaite (n = 4)	SO4red300 Pentlandite (n = 1) ^a	SO4red328 Chrysotile (n = 11)	SO4red 328 Brucite (n = 2)	SO4red328 Valleriite (n = 4)	SO4red328 Ni,Fe-sulfide (n = 1) ^a
SiO ₂	40.6	29.4 (1.1)	0.13 (0.09)	4.7 (2.7)	1.4	29.9 (1.4)	3.0 (1.8)	1.8 (1.1)	0.3
TiO ₂	b.d.	b.d.	b.d.	b.d.	b.d.	b.d.	b.d.	b.d.	b.d.
Al ₂ O ₃	0.03	0.51 (0.16)	b.d.	1.4 (0.2)	b.d.	1.0 (0.1)	b.d.	2.7 (0.7)	b.d.
Cr ₂ O ₃	b.d.	b.d.	b.d.	b.d.	b.d.	b.d.	b.d.	b.d.	b.d.
FeO	8.9	2.1 (0.1)	2.8 (0.2)	28.1 (1.2)	27.1	1.9 (0.4)	1.0 (0.6)	27.1 (3.7)	9.5
MgO	50.1	28.8 (2.5)	70. (5)	18.3 (3.0)	1.8	29.1 (1.5)	61. (0.4)	16.8 (2.6)	2.1
MnO	0.14	0.03 (0.02)	0.19 (0.04)	b.d.	b.d.	–	–	–	–
CaO	0.07	0.06 (0.02)	b.d.	b.d.	b.d.	b.d.	b.d.	b.d.	b.d.
Na ₂ O	–	0.16 (0.09)	b.d.	b.d.	b.d.	b.d.	b.d.	b.d.	b.d.
K ₂ O	–	b.d.	b.d.	b.d.	b.d.	b.d.	b.d.	b.d.	b.d.
NiO	0.38	0.06 (0.04)	b.d.	18.6 (0.8)	49.1	0.09 (0.04)	b.d.	5.1 (2.4)	67.4
CoO	–	b.d.	b.d.	0.14 (0.05)	4.2	b.d.	–	b.d.	1.0
Cu ₂ O	–	b.d.	b.d.	0.14 (0.05)	4.2	b.d.	–	13.2 (2.4)	b.d.
S	–	b.d.	b.d.	18.4 (1.1)	30.8	0.21 (0.05)	0.3 (0.2)	19.1 (3.1)	35.1
Cl	–	0.69 (0.19)	b.d.	0.19 (0.05)	b.d.	–	b.d.	–	–
Total	100.1	62 (5)	73 (5)	89.9 ^b (4.4)	115 ^b	62 (3)	65 (3)	86 ^b (11)	115 ^b
Mg#	91	96 (1)	98 (0)	–	–	96 (1)	99 (1)	–	–
(Mg+Fe)/Si ^c	2.0	1.5 (<0.1)	–	–	–	1.5 (<0.1)	–	–	–
(Fe+Ni+Cu+Co)/S ^c	–	–	–	1.12 (0.03)	1.1	–	–	1.04 (0.11)	0.95

Notes: – = not measured or not applicable; b.d. = Below detection limit of ~0.05 wt%; SC = San Carlos.

^aOwing to the small crystal size (<1 µm) and close association with other phases, it was difficult to obtain reliable EMPA results for pentlandite and Ni,Fe-sulfide. The compositions shown here represent what appear to be the most reliable individual analyses.

^bThe totals for pentlandite and Ni,Fe-sulfide exceed 100 wt% because Fe, Ni, Cu, and Co are reported in the table as oxides although they are present as sulfides in the mineral. Similarly, the totals for haapalaite and valleriite are likely to be high since no correction is made for the amounts of metals that are present in the sulfide layers rather than the hydroxide layers.

^cMolar ratios.

a beam current of 10 nA, and a 1 μm beam diameter. Raman spectroscopy was performed using a Horiba LabRAM HR confocal spectrometer with either a 633 nm laser (chrysotile and brucite) or 532 nm laser (valleriite and haapalaite).

Thermogravimetric analysis (TGA) was conducted using a Thermal Analysis Instruments SDT Q600 instrument, with samples placed in an alumina crucible and heated from room temperature to 1100 $^{\circ}\text{C}$ at 10 $^{\circ}\text{C}$ per minute while monitoring the change in mass and heat flow. Mössbauer spectroscopy (MS) was performed at room temperature using a conventional constant-acceleration spectrometer (model MS6, SeeCo, U.S.A.) in transmission geometry with a $^{57}\text{Co}/\text{Rh}$ source. A vibrating sample magnetometer (Model 3900, Princeton Corporation Measurements) was used to obtain room-temperature hysteresis parameters on the reacted solids, including the saturation magnetization (M_s). The weight percent of magnetite in the reacted solids was then determined from the M_s of the sample and the known value for pure magnetite ($M_s = 92 \text{ Am}^2/\text{kg}$) with the equation:

$$\text{wt\% magnetite} = [M_s(\text{sample})/M_s(\text{magnetite})] \times 100. \quad (1)$$

The sulfur isotopic compositions of dissolved sulfate and solid materials were analyzed using a Thermo Delta C Plus isotope-ratio mass spectrometer (IRMS). The isotopic composition of dissolved sulfate was performed by addition of barium chloride to a fluid aliquot followed by combustion of the resulting barium sulfate, using a set of calibration standards prepared by diluting the initial ^{34}S -labeled artificial seawater solution with natural abundance sulfate. The olivine and FeS used as reactants were combusted with a Costech ECS 4010 Elemental Analyzer and the products measured using thermal conductivity for sulfur abundance and using IRMS for sulfur isotopic composition. After completion of the experiments, remaining sulfate minerals were removed from the solid products and the chromium-reducible sulfur (CRS) component of the solids was extracted and purified as silver sulfide following methods described in Houghton et al. (2022). The isotopic composition of the silver sulfide yield was analyzed by IRMS using the same calibration methods as the ^{34}S -labeled barium sulfate precipitates. Sulfur isotope compositions are expressed in standard delta notation as per mil (‰) deviations from the Vienna Canyon Diablo Troilite (VCDT) standard.

Calculations to estimate in situ pH were performed with the computer program EQ3 (Wolery and Jarek 2003). The calculations involved two steps. First, fluid speciation calculations were performed at 25 $^{\circ}\text{C}$ using the measured fluid compositions including the room temperature pH, and adjusting for charge balance with Na. The total dissolved Na calculated at 25 $^{\circ}\text{C}$ was then used with other measured concentrations to re-speciate the fluid at the reaction temperature, with charge balance determining the in situ pH. The calculations were performed for a pressure of 35 MPa using the customized database described in McCollom and Bach (2009).

RESULTS

Fluid composition

Changes in fluid compositions during the experiments are illustrated in Figure 1, with complete measurements listed in Table 2. Also included in Figure 1 for comparison are results from previous olivine-only serpentinization experiments performed at comparable temperatures using the same methods, but with a NaCl solution rather than artificial seawater as the reactant fluid (McCollom et al. 2016). Because these previous experiments did not include dissolved sulfate or added sulfide minerals among the reactants, they are essentially sulfur free. The previous experiments also utilized olivine with a larger particle size (53–212 μm) resulting in somewhat slower rates of serpentinization.

The onset of heating resulted in steep decreases in ΣSO_4 and Mg concentrations in both experiments, and Ca concentrations also decreased sharply to $\sim 2.5 \text{ mmol kg}^{-1}$ in the early stages of SO4red328 (Figs. 1c and 1g; Table 2). The decreased concentrations of these components are likely attributable to precipitation of anhydrite and magnesium hydroxide sulfate hydrate (MHSH) during heating, as reported in other serpentinization experiments performed under similar conditions (e.g., Janecky and Seyfried 1986). The concentrations of ΣSO_4 and Mg (and Ca in SO4red328) remained low during the remainder of heating, but then increased sharply after the experiments were ended and returned to room

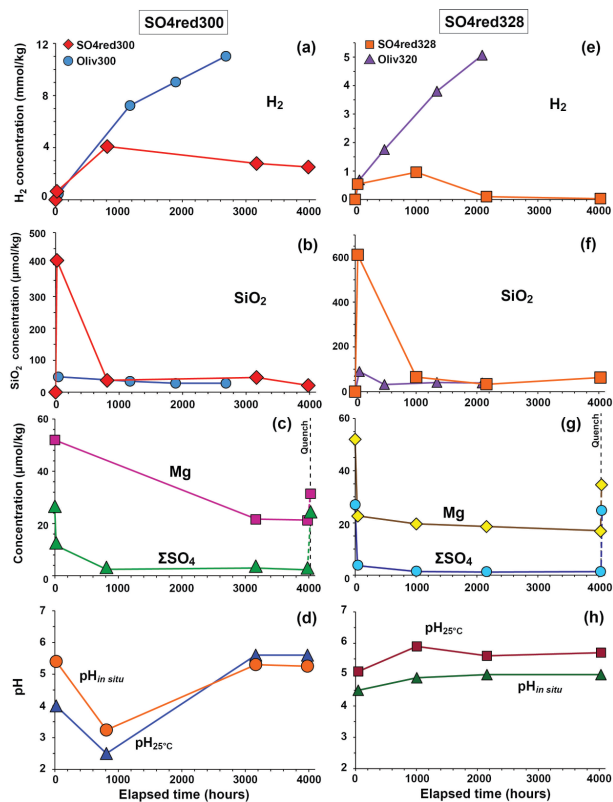


FIGURE 1. Evolution of fluid compositions during (a–d) SO4red300 and (e–h) SO4red328. In a, b, e, and f, results for other olivine serpentinization experiments that lacked sulfate are shown for comparison, while other panels show only results for the present experiments. (a and e) Dissolved concentrations of H_2 . (b and f) Total dissolved SiO_2 . (c and g) Dissolved Mg and ΣSO_4 . Last measurements were acquired after the experiments were cooled to room temperature (quench; indicated by dashed black lines). (d and h) Measured room temperature pH ($\text{pH}_{25^{\circ}\text{C}}$) and calculated in situ pH ($\text{pH}_{\text{in situ}}$). Data for Oliv300 and Oliv320 are from McCollom et al. (2016). (Color online.)

temperature (Figs. 1c and 1g). These increases can be attributed to dissolution of sulfate minerals that formed earlier in the experiments as the reaction vessel cooled. At 300 $^{\circ}\text{C}$, dissolved Na, Ca, and K all maintained levels close to their original concentrations throughout the experiment, while Fe increased from below detection to 0.2 mmol kg^{-1} with increased reaction time (Table 2). At 328 $^{\circ}\text{C}$, dissolved Fe initially increased sharply to 2.3 mmol kg^{-1} and then steadily decreased to $150 \text{ }\mu\text{mol kg}^{-1}$ (Table 2). Nickel was at or below the detection limit of $2 \text{ }\mu\text{mol kg}^{-1}$ in all samples.

Molecular hydrogen (H_2) is a characteristic by-product of serpentinization reactions (e.g., McCollom et al. 2016, 2020), and generation of H_2 began immediately with the onset of heating for both experiments (Figs. 1a and 1e). However, in contrast to the steadily increasing H_2 levels observed in other olivine experiments performed without SO_4 present, the measured H_2 concentrations decreased after 813 h in SO4red300 and after 1004 h in SO4red328. The decreasing H_2 concentrations in these experiments are largely attributable to consumption of H_2 during reduction of dissolved sulfate to H_2S , most of which subsequently precipitated as sulfur-bearing minerals. The concentration of $\Sigma\text{H}_2\text{S}$ was below detection

TABLE 2. Fluid compositions during the experiments

Time (h)	T (°C)	H ₂ (m)	CO ₂ (m)	CH ₄ (μ)	Na (m)	Cl (m)	ΣSO ₄ (m)	δ ³⁴ S SO ₄	ΣH ₂ S (μ)	SiO ₂ (μ)	Mg (m)	Ca (m)	K (m)	Fe (μ)	Cu (μ)	Ni (μ)	pH (25 °C)	pH in situ	Fluid ^a (g)
Experiment SO4red300																			
Initial 0	18	0	2.3	0	462	543	26.6	4750	0	0	52	9.2	9.3	0	0	0	8.2	–	–
	Start of experiment at 300 °C																		
21	300	0.64	5.5	18	–	475	12.6	–	b.d.	410	–	–	–	–	–	–	4.0	5.4	38.1
813	300	4.1	5.5	83	–	463	3.2	–	b.d.	37	–	–	–	–	–	–	2.5	3.2	34.7
3165	300	2.8	3.5	73	442	478	3.7	–	100	46	22	11	11	64	12	<2	5.6	5.3	30.3
3981	300	2.5	5.6	120	436	467	3.0	–	270	21	21	10	10	200	5	<2	5.6	5.3	25.9
4001 Experiment terminated and cooled to room temperature																			
4025	20	–	–	–	437	470	24.5	–	–	–	31	10	10	3.5	2	<2	8.0	–	18.1
Experiment SO4red328																			
Initial 0	18	0	2.3	0	462	543	26.6	4790	0	0	52	9.2	9.3	0	0	0	8.2	–	–
	Start of experiment at 328 °C																		
43	328	0.54	5.1	48	411	–	3.9	–	b.d.	610	23	9.5	9.8	2300	<2	<2	5.1	4.5	37.6
1004	328	0.96	4.1	211	472	–	1.6	–	400	65	20	2.7	12	270	19	<2	5.9	4.9	31.8
2156	328	0.10	4.2	287	457	–	1.4	–	700	33	19	2.7	12	140	<2	<2	5.6	5.0	29.4
4028	326	0.03	4.6	361	442	–	1.4	–	770	63	17	2.4	11	150	9	<2	5.7	5.0	24.0
4030 Experiment terminated and cooled to room temperature																			
4044	20	–	–	–	441	–	24.8	4720	–	110	35	11	11	70	18	<2	–	–	17.0

Notes: Concentrations in mmol kg⁻¹ (m) or μmol kg⁻¹ (μ). b.d. = below detection limit; – = not determined.

^aAmount of fluid in reaction cell prior to sampling.

in the first couple of fluid samples from SO4red300 but rose to detectable levels as the experiment progressed, attaining a final concentration of 270 μmol kg⁻¹ (Table 2). Increasing levels of ΣH₂S were also observed as the reaction progressed in SO4red328, attaining a somewhat higher final concentration of 770 μmol kg⁻¹ (Table 2).

The ΣSO₄ in the reactant solution was purposely enriched in ³⁴S, with an initial isotopic composition of 4749 ± 5‰ and 4790 ± 5‰ in SO4red300 and SO4red328, respectively (Table 2). When the reaction vessel was cooled following termination of SO4red328, the isotopic composition of dissolved ΣSO₄ was confirmed to be 4719 ± 20‰ (Table 2). To assess the degree to which the label was incorporated into ΣH₂S, the headspace from a gas-tight syringe obtained during the final fluid sample of SO4red328 at 4028 h was injected into a GC-MS, with results displayed in Figure 2. Comparison of the experiment sample with a calibration gas standard containing natural abundances of S isotopes shows that the ΣH₂S from SO4red328 had substantially higher abundances of ions with mass-to-charge ratios (m/z) of 35 and 36 than the standard, indicating substantial enrichment of the sample in H₂³⁴S from the labeled sulfate (Fig. 2). Although the results are semiquantitative, calculations based on the GC-MS results suggests that the ΣH₂S from SO4red328 had roughly the same proportion of ³⁴S as the dissolved ΣSO₄.

The concentration of ΣSiO₂ in SO4red300 increased sharply to 410 μmol kg⁻¹ during the first day of heating, but then decreased to much lower levels (30 ± 10 μmol kg⁻¹) for the remainder of the experiment (Fig. 1b). A similar pattern was observed in SO4red328, where the ΣSiO₂ concentration initially increased to 610 μmol kg⁻¹ before leveling off between 33 and 65 μmol kg⁻¹ (Fig. 1f). In both cases, the low ΣSiO₂ were similar to those observed in other, sulfate-free olivine serpentinization experiments (Figs. 1b and 1f).

The room temperature pH (pH_{25°C}) became mildly acidic in the early stages of SO4red300, but became less acidic with continued heating (Fig. 1d). The calculated in situ pH (pH_{in situ}) was also mildly acidic early in the experiment, but approached circumneutral conditions during the latter stages (neutral pH at the experimental conditions is 5.5). Both pH_{25°C} and pH_{in situ} were mildly acidic in SO4red328 as well (Fig. 1h).

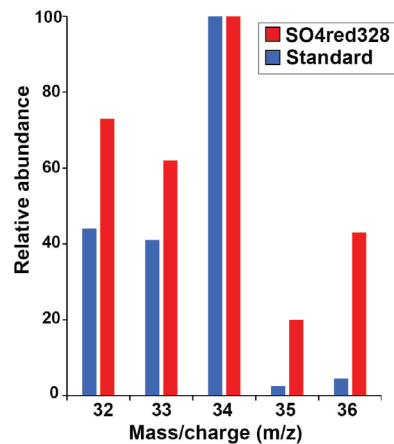


FIGURE 2. Relative abundances of fragments with different mass/charge ratios (m/z) produced during gas chromatography-mass spectrometry analysis of ΣH₂S from SO4red328 compared with those from an H₂S calibration standard analyzed with the same method. Results of both samples are normalized to the abundance of the m/z = 34 fragment. The sample was obtained after 4028 h of reaction. (Color online.)

Solid products

The solids recovered from both experiments after reaction are dominated by serpentine together with relict olivine (Fig. 3; Online Materials¹ Fig. S3). Magnetite and brucite are also present as minor secondary products in both experiments. The serpentine has a fibrous texture, suggesting that it is mainly chrysotile, and it yielded Raman spectra similar to chrysotile from other laboratory experiments performed under comparable conditions (Online Materials¹ Fig. S4). Analysis of the reaction products by EMPA (Table 1) indicated that the serpentine from both experiments has similar compositions with an Mg# = 96 [Mg# = 100 × Mg/(Mg+Fe), molar basis]. Brucite primarily occurs as dispersed clusters of crystals with a thin, tabular habit and diameters commonly >100 μm and thicknesses <4 μm (e.g., Fig. 3c; Online Materials¹ Fig. S5), which are similar to brucite observed in other serpentinization experiments conducted under comparable conditions (e.g., McColom et al. 2016, 2020). The brucite from SO4red300 has a Mg#

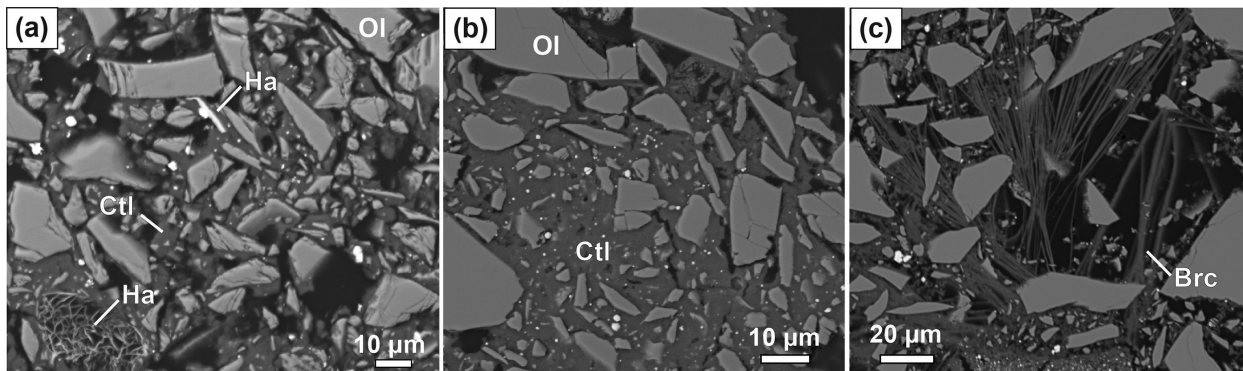


FIGURE 3. Backscattered electron images of reacted solids from experiments. (a) Reaction products from SO4red300, including relict olivine (light gray; Ol) embedded in mat of chrysotile (dark gray; Ctl). Bright haapalaite crystals (Ha) are labeled, with one crystal associated with pentlandite (Fig. 4c). Most other bright spots are magnetite. (b) Reaction products from SO4red328, with dense mat of chrysotile fibers and magnetite surrounding partially reacted olivine. (c) Cross section of large, tabular brucite crystals (medium gray; Brc) from SO4red328. Note that because the brucite occurs as thin, platy minerals (e.g., Online Materials¹ Fig. S5), they appear acicular in this cross section.

= 98 while that from SO4red328 has an Mg# = 99. In both of the experiments, the serpentine and brucite are depleted in Fe relative to the olivine reactant (Mg# = 90), reflecting the partitioning of some Fe into magnetite. Based on magnetization measurements, magnetite comprises 0.68 wt% of the reacted solids in SO4red300 and 0.71 wt% in SO4red328.

Examination of the reacted solids recovered from both experiments by SEM also revealed trace amounts of thin, tabular minerals with hexagonal terminations (Fig. 4). The habit of these minerals resembled that of brucite, albeit with much smaller dimensions than the brucite present in the reacted solids (i.e., diameters <20 µm for the platy minerals vs. >100 µm for brucite; compare Figs. 3e and 4). In contrast to brucite, however, initial analysis of the smaller tabular minerals by EDS indicated that they contained substantial amounts of S as well as much higher amounts of metallic elements than the coexisting brucite. Subsequent analysis by EMPA revealed that the tabular minerals have chemical compositions that require the presence of both sulfide and oxide/hydroxide components in the mineral structure (Table 1). These compositions are consistent with members of the tochilinite-valleriite group (Table 1; Online Materials¹ Table S1). More specifically, the tabular minerals in SO4red300 have Fe- and Ni-rich compositions consistent with the mineral haapalaite, while those in SO4red328 have Fe- and Cu-rich compositions consistent with valleriite (Table 1; Online Materials¹ Table S1). The tabular, hexagonal crystal habit is also consistent with haapalaite and valleriite (e.g., Huhma et al. 1973; Mikhlin et al. 2022a). Peaks corresponding to TVG minerals are not apparent in XRD patterns of the reaction products (Online Materials¹ Fig. S3); however, this is not unexpected given that the trace amounts of these minerals present in the reacted solids would be well below the detection limit for that method (~3 wt%).

Because the distribution of cations between the sulfide and hydroxide layers of the TVG minerals could not be uniquely determined from EMPA alone, it is not possible to assign a precise chemical formula to these minerals. However, the results indicate the minerals in SO4red328 have a molar (Fe+Cu+Ni):S ratio of about 1.04 and while those in SO4red300 have a ratio of ~1.12, both of which are greater than the ratio near one expected for the sulfide layer of TVG minerals (Table 1; Online Materials¹ Table S1). It is therefore likely that some fraction of the Fe, and possibly some

of the Cu and Ni, resides in the hydroxide layers rather than the sulfide layers. The measured compositions also included small and variable amounts of SiO₂ (Table 1), although this could be at least partially attributable to chrysotile intergrown with the TVG minerals (e.g., Zolensky and MacKinnon 1986). Assuming that: (1) The $\Sigma(\text{Fe}+\text{Cu}+\text{Ni}):S$ ratio in the sulfide layer is equal to one; (2) the SiO₂ resides in chrysotile impurities intergrown with the TVG minerals; and (3) all of the Mg and Al are limited to the hydroxide layers, mass-balance calculations indicate that the measured composition of the valleriite in SO4red328 is consistent with a chemical formula of $2(\text{Fe}_{0.58}\text{Cu}_{0.31}\text{Ni}_{0.11})\text{S} \cdot 1.53(\text{Mg}_{0.81}\text{Fe}_{0.08}\text{Al}_{0.11})\text{OH}_2$ while that of haapalaite in SO4red300 is $2(\text{Fe}_{0.58}\text{Ni}_{0.42})\text{S} \cdot 1.50(\text{Mg}_{0.77}\text{Fe}_{0.16}\text{Al}_{0.07})\text{OH}_2$. In both cases, the hydroxide layers appear to contain substantially higher Fe contents than coexisting brucite (which has compositions near $(\text{Mg}_{0.98}\text{Fe}_{0.02})\text{OH}_2$ in both experiments).

Table 3 compares the molecular formulas of the minerals from the experiments with those reported for valleriite and haapalaite from several natural occurrences, most of which are in serpentinites. The composition of minerals from SO4red328 is consistent with natural samples of valleriite, albeit the experimental products contain somewhat lower Cu and higher Ni than those reported from natural settings. Valleriite from natural serpentinites exhibit substantial variability in chemical composition (see also Mücke 2017). The lower Cu and higher Ni in the products from SO4red328 appears to be an extension of that variability, which most likely reflects a somewhat different chemical environment in the experiment than in the natural systems. Fewer data are available for Ni-rich TVG minerals in natural settings, but the composition of the minerals from SO4red300 is very similar to that of haapalaite from the type locality in Finland (Table 3).

Raman spectroscopy was employed to further assess the identity of the experimental products (Fig. 5). The Raman spectrum for the tabular minerals from SO4red328 is very similar to a reference spectrum for natural valleriite from the RRUFF database, and resembles even more closely a Raman spectrum for synthetic valleriite (Fig. 5; note that the synthetic valleriite shown in the figure has Fe:Cu ratio close to one and a mixture of Mg and Al in the hydroxide layer, similar to the SO4red328 products). Both the minerals from SO4red328 and the reference spectra exhibit two broad, prominent maxima at ~283 and ~336 cm⁻¹. The similarity in Raman spectra,

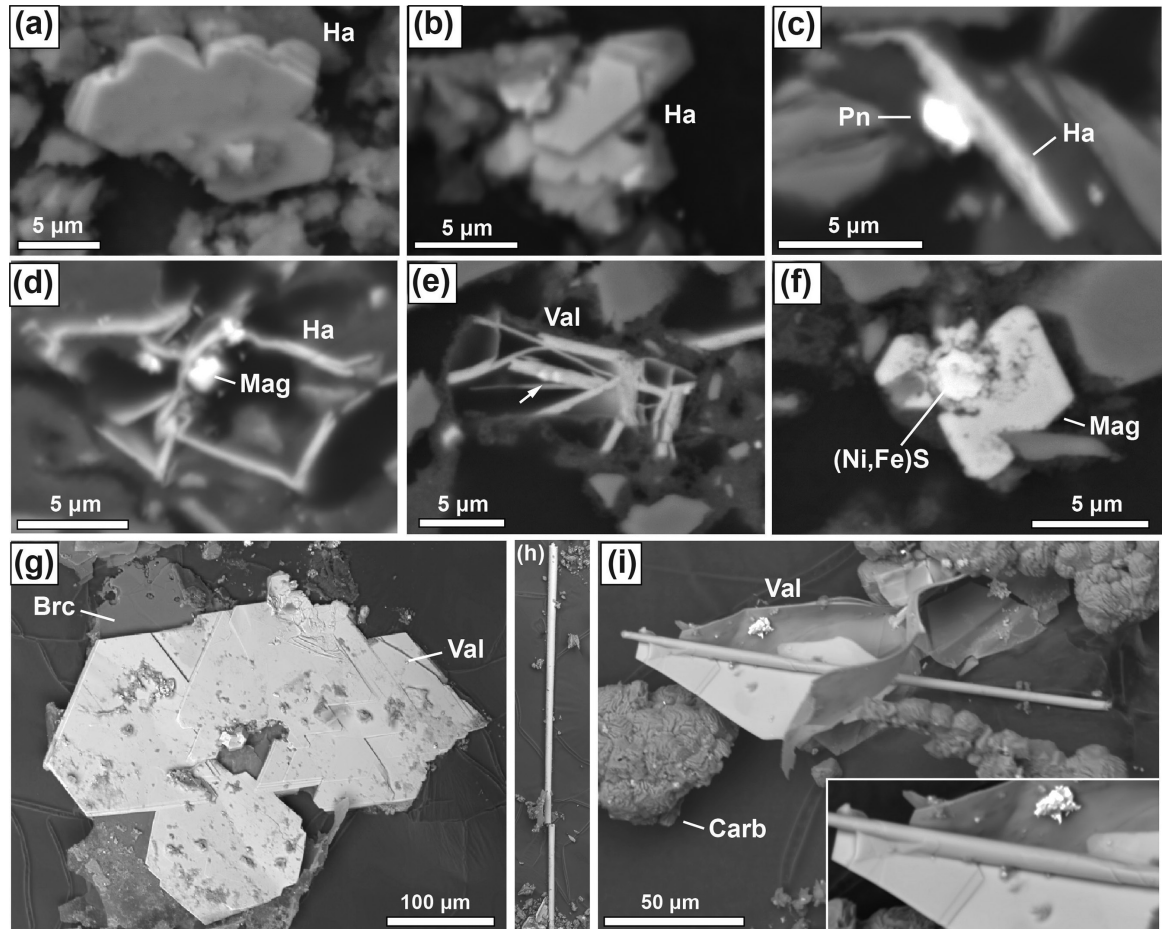


FIGURE 4. Backscattered electron images showing examples of TVG minerals and sulfides formed during the serpentinization experiments. (a–d) Haapalaite (Ha) formed in SO4red300. Note pentlandite (Pn) adjacent to haapalaite crystal in (c); see Figure 2a for context of this image. (e) Cluster of vallerite crystals (Val) from SO4red328. The arrow points to small inclusions of Ni,Fe-sulfide in the valleriite (bright spots). (f) Ni,Fe-sulfide crystal embedded within magnetite. Elemental maps corresponding to this image are provided as Online Materials¹ Figure S7. (g, h, and i) Vallerite crystals precipitated on closure piece of reaction cell. In g, the vallerite precipitated directly onto a large brucite crystal (Brc). Images h and i show acicular habit of some vallerite crystals, with inset in i showing an expanded view where the vallerite appears to transition from tabular to acicular morphology. The length of the vallerite crystal in h is ~600 μ m. Images (a, b, g, h, and i) are from grains mounted on carbon tape while (c–f) show minerals in cross section from polished thin-sections. Carb = carbonate minerals.

combined with the chemical composition and crystal morphology, indicates that the experimental products from SO4red328 can be identified as vallerite with a high degree of confidence. To our knowledge, there is no alternative to vallerite that could possibly account for the combination of chemical composition, morphology, and Raman spectrum observed for the minerals from SO4red328.

No reference Raman spectrum could be found for haapalaite. The Raman spectra for tabular minerals from SO4red300 exhibit two broad, prominent maxima, analogous to the two prominent maxima that dominate the spectra for vallerite and tochilinite (Fig. 5). The positions of the maxima for the SO4red300 products, however, have a substantially lower Raman shift than vallerite, and are intermediate between those of vallerite and tochilinite. The maxima in the Raman spectra for TVG minerals are evidently attributable to vibrations of metallic element-S bonds (e.g., Mikhlin et al. 2022a), hence it is reasonable to expect that the position and shape of the maxima may vary as a function of the relative abundances and

oxidation states of Fe, Cu, and Ni in the sulfide layer [note that the reference tochilinite spectrum shown in Fig. 5 evidently represents a pure Fe end-member; see similar spectra in Vacher et al. (2017)]. The lower Raman shift of the maxima observed for the SO4red300 products relative to vallerite may therefore reflect differences in the relative abundances of Ni, Cu, and Fe that led to variation in the structure of the sulfide layer. If the tabular minerals from SO4red300 are indeed haapalaite (as indicated by the chemical composition, morphology, and overall similarity to the vallerite from SO4red328), then the Raman spectrum shown in Figure 5 may represent the first published spectrum for this mineral. Lastly, it is worth noting that despite the presence of brucite-like hydroxide layers in the structure of TVG minerals (e.g., Organova et al. 1971, 1974; Mikhlin et al. 2022a), none of the minerals from this group exhibits an OH stretch feature at ~3650 cm^{-1} like that observed for brucite (Fig. 5).

For the most part, the TVG minerals observed in the

TABLE 3. Comparison of molecular formulas for valleriite and haapalaite from laboratory experiments compared with minerals in natural serpentinites

Experiment or Locality	Formula	Reference
SO4red328	$2(\text{Fe}_{0.59}\text{Cu}_{0.30}\text{Ni}_{0.11})\text{S}\cdot1.53(\text{Mg}_{0.81}\text{Fe}_{0.08}\text{Al}_{0.11})\text{OH}_2$	This study
Del Norte, California	$2(\text{Fe}_{0.67}\text{Cu}_{0.33})\text{S}\cdot1.49(\text{Mg}_{0.68}\text{Fe}_{0.18}\text{Al}_{0.16})\text{OH}_2$	1
Kaveltorp, Sweden	$2(\text{Fe}_{0.57}\text{Cu}_{0.43})\text{S}\cdot1.49(\text{Mg}_{0.77}\text{Al}_{0.23})\text{OH}_2$	2
Kaveltorp, Sweden	$2(\text{Fe}_{0.58}\text{Cu}_{0.42})\text{S}\cdot1.68(\text{Mg}_{0.72}\text{Al}_{0.28})\text{OH}_2$	2
Kaveltorp, Sweden	$2(\text{Fe}_{0.60}\text{Cu}_{0.40})\text{S}\cdot1.56(\text{Mg}_{0.83}\text{Fe}_{0.17})\text{OH}_2$	3
Kingash, Siberia	$2(\text{Fe}_{0.53}\text{Cu}_{0.47})\text{S}\cdot1.47(\text{Mg}_{0.64}\text{Fe}_{0.24}\text{Al}_{0.12})\text{OH}_2$	4
Loolekop, South Africa	$2(\text{Fe}_{0.47}\text{Cu}_{0.53})\text{S}\cdot1.92(\text{Mg}_{0.64}\text{Fe}_{0.08}\text{Al}_{0.27})\text{OH}_2$	2
Loolekop, South Africa	$2(\text{Fe}_{0.52}\text{Cu}_{0.47})\text{S}\cdot1.53(\text{Mg}_{0.66}\text{Al}_{0.23})\text{OH}_2$	5
Palabora, South Africa	$2(\text{Fe}_{0.48}\text{Cu}_{0.52})\text{S}\cdot1.67(\text{Mg}_{0.75}\text{Fe}_{0.16}\text{Al}_{0.09})\text{OH}_2$	3
IODP Hole 1068A, Iberia margin	$2(\text{Fe}_{0.59}\text{Cu}_{0.30}\text{Ni}_{0.04})\text{S}\cdot2.76(\text{Mg}_{0.53}\text{Fe}_{0.41}\text{Al}_{0.06})\text{OH}_2$	6
Yukon, Canada	$2(\text{Fe}_{0.40}\text{Cu}_{0.60})\text{S}\cdot1.64(\text{Mg}_{0.71}\text{Fe}_{0.06}\text{Al}_{0.23})\text{OH}_2$	7
Akagane Mine, Japan	$2(\text{Fe}_{0.42}\text{Cu}_{0.58})\text{S}\cdot1.76(\text{Mg}_{0.82}\text{Al}_{0.19})\text{OH}_2$	8
Noril'sk, Siberia	$2(\text{Fe}_{0.50}\text{Cu}_{0.50})\text{S}\cdot1.47\text{FeOH}_2$	5
Valleriites		
SO4red300	$2(\text{Fe}_{0.58}\text{Ni}_{0.42})\text{S}\cdot1.50(\text{Mg}_{0.77}\text{Fe}_{0.16}\text{Al}_{0.07})\text{OH}_2$	This study
Outokumpu, Finland ^a	$2(\text{Fe}_{0.63}\text{Ni}_{0.37})\text{S}\cdot1.63(\text{Mg}_{0.68}\text{Fe}_{0.14}\text{Al}_{0.01})\text{OH}_2$	9
IODP Hole 1068A, Iberia margin	$2(\text{Fe}_{0.74}\text{Ni}_{0.26})\text{S}\cdot1.86(\text{Mg}_{0.70}\text{Fe}_{0.15}\text{Al}_{0.16})\text{OH}_2$	6
IODP Hole 1068A, Iberia margin	$2(\text{Fe}_{0.78}\text{Ni}_{0.22})\text{S}\cdot1.84(\text{Mg}_{0.74}\text{Fe}_{0.09}\text{Al}_{0.17})\text{OH}_2$	6
Haapalaites		

Notes: References: (1) Harris and Vaughan (1972); (2) Evans and Allmann (1968); (3) Springer (1968); (4) Mikhlin et al. (2022b); (5) Harris et al. (1970); (6) Beard (2000); (7) Petruk et al. (1971); (8) Matsubara and Kato (1992); (9) Huhma et al. (1973). ^aType locality.

experimental products were small tabular crystals embedded among the other products of serpentinization, with thicknesses mostly ~ 1 μm and diameters up to about 15 μm across (Figs. 4a–4e). In SO4red328, however, a few much larger valleriite crystals precipitated on the titanium closure piece of the reaction cell with diameters up to several hundred μm (i.e., Fig. 4g). While the majority of the crystals throughout the sample had a tabular habit, a couple of the valleriite crystals found on the closure piece had an acicular habit and, in one case, appeared to be transitioning from tabular to acicular morphology (Figs. 4h and 4i). Tochilinite is known to have both tabular and acicular habits (Organova et al. 1973, 1974; Zolensky and MacKinnon 1986), although the tabular

habit appears to be more common in natural serpentinite. Although the larger crystals found on the closure piece were not analyzed by EMPA, there was no detectable difference in the composition of these crystals and those found in the bulk solids using EDS.

Confirmation that S in the TVG minerals was present in a reduced state (i.e., sulfide rather than sulfate) was obtained by measuring the centroid of the $\text{SK}\alpha$ emission line via wavelength-dispersive X-ray spectroscopy (WDS) scans. The energies of X-rays emitted from S-bearing minerals and glasses have been shown to vary systematically as a function of the formal valence of sulfur (Carroll and Rutherford 1988; Wallace and Carmichael 1994). This is illustrated in Figure 6, which shows beam-current normalized WDS scans for the mineral identified as haapalaite from SO4red300 compared with pentlandite and anhydrite standards. The $\text{SK}\alpha$ peak centroid for the pentlandite standard occurs at 2307.4 eV while that for anhydrite occurs at 2308.8 eV. The energy of the $\text{SK}\alpha$ centroid for the haapalaite is nearly identical to that of the pentlandite standard, confirming that S is present in the S^{II} oxidation state.

As an aside, it should be noted that the chemical compositions of TVG minerals listed in Table 1 represent only the best quality EMPA results. The small size (mostly ~ 1 μm thick; Fig. 4) of the TVG crystals as well as their close spatial association with chrysotile or other minerals precluded accurate determination of their compositions for most crystals, resulting in low totals and high SiO_2 contents. Although lower quality data are excluded from the average compositions listed in Table 1, in all cases the lower quality analyses were consistent with the compositions shown in the table and there was no indication that there was significant compositional variability of the TVG minerals within the individual experiments.

Other trace minerals found sparsely distributed among the reacted solids included sulfides, prismatic Ca-sulfate minerals (presumably anhydrite; Online Materials¹ Fig. S6), and Mg-Ca carbonates (presumably dolomite; e.g., Fig. 4i). In SO4red300, the sulfides included both individual crystals that contain predominantly Fe and others that contain substantial amounts of Ni and Co in addition to Fe. The very small size of the sulfides (predominantly <1 μm diameter) precluded accurate determination of their identity by Raman spectroscopy or of their composition by EMPA. However, the most

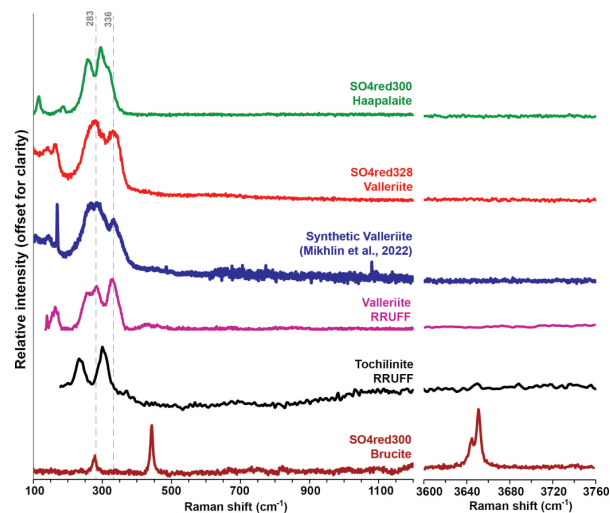


FIGURE 5. Raman spectra of TVG minerals and brucite from the laboratory experiments with reference spectra shown for comparison. The reference spectra include natural valleriite and tochilinite from the RRUFF database and a synthetic valleriite from Mikhlin et al. (2022a). No reference spectrum could be found for haapalaite. Additional Raman results for serpentine and brucite are shown in Online Materials¹ Figure S4. Raman data for the experimental products are provided as Data Set 1. (Color online.)

reliable measurements for the Ni-bearing sulfides in SO4red300 resulted in an approximate chemical formula of $\text{Ni}_{5.4}\text{Fe}_{3.2}\text{Co}_{0.5}\text{S}_8$ (Table 1). Based on this composition, the Ni-bearing sulfide in that experiment is most likely pentlandite (cf. Klein and Bach 2009). The pentlandite contains proportionally greater amounts of Ni and Co than the sulfide layers of the haapalaite in the same experiment (see molecular formula above).

The Fe-sulfides found in SO4red300 could be remnants of the pyrrhotite included among the initial reactants. However, low-temperature magnetization measurements (20–300 K) detected the magnetic transition for magnetite (Verwey transition at ~120 K) but did not show evidence for the magnetic association associated with pyrrhotite (Besnus transition at ~34 K) at a detection limit of ~0.01 wt%, suggesting that most of the original pyrrhotite reacted during the experiment. Furthermore, the size of the Fe-sulfides in the reaction products is significantly smaller than the added reactant FeS. Accurate compositional analyses of the Fe-sulfide particles in the reaction products could not be obtained by EPMA, so their identity is uncertain.

The Ni-bearing sulfides in SO4red328 had significantly higher Ni:(Ni+Fe) and lower (Ni+Fe):S ratios than the pentlandite found in SO4red300, and Co levels were substantially lower (Table 1). Based on a (Ni+Fe):S value close to one and Ni:(Ni+Fe) ≈ 0.87, these minerals could be crowningshieldite or millerite rather than pentlandite. However, because the identification is uncertain, this phase is referred to here as (Ni,Fe)-sulfide. In several instances (Ni,Fe)-rich sulfides were observed to be enshrouded by larger magnetite crystals (Fig. 4f; Online Materials¹ Fig. S7). A few particles of an Fe,Zn-sulfide were also observed in SO4red328, but no pure-Fe sulfides were found in this experiment. In addition, a few crystals of a Cu-sulfide mineral with a Cu:S ratio near one were found during inspection of the reaction products of SO4red328 (Online Materials¹ Fig. S8).

In some instances, sulfide minerals and magnetite were observed in close proximity to the TVG minerals in both experiments (Figs. 4 and 7). In other cases, however, TVG minerals were found with no adjacent sulfides or magnetite, and many sulfide and mag-

netite crystals were not associated with TVG minerals. Thus, there is no consistent evidence that the TVG minerals were produced by alteration of preexisting sulfides or magnetite; rather, all of these minerals appear to be co-precipitating from solution.

The isotopic composition of the chromium-reducible sulfur (CRS) fraction of the bulk solids, which presumably reflects the bulk reduced S in the reaction products, was $2159 \pm 176\text{‰}$ in SO4red300 and $3266 \pm 256\text{‰}$ in SO4red328. These values reflect contributions from both the labeled sulfate added to the reactant solution ($\delta^{34}\text{S}_{\text{SO}_4} \approx 4749$ or 4790‰ , respectively) and a natural abundance sulfur source. In the case of SO4red300, the pyrrhotite added to the initial reactants had an isotopic composition of $\delta^{34}\text{S}_{\text{FeS}} = 14.2 \pm 0.3\text{‰}$. In addition, the powdered olivine used in the experiments was found to contain a small amount of S (0.018 wt%), of which 26% is recoverable in CRS with a $\delta^{34}\text{S}_{\text{olivine}}$ value of $0.4 \pm 0.3\text{‰}$. Since SO4red328 lacked added FeS, the source of the natural abundance sulfur is most likely the trace reduced S in the olivine reactant. The very heavy isotopic compositions of the CRS fractions from the reacted solids indicate a substantial contribution of ^{34}S from the labeled ΣSO_4 to the reduced S fraction.

Thermogravimetric analysis (TGA) of the reacted solids showed mass losses attributable to serpentine and brucite (Online Materials¹ Fig. S9; cf. Klein et al. 2020). The TGA results indicate that the reacted solids from SO4red300 contain 13.0 wt% chrysotile and 0.75 wt% brucite that, combined with the magnetite abundance, equates to a reaction of about 12.8% of the original olivine during the experiment (Table 4). The products of SO4red328 contain 14.8 wt% chrysotile, 0.79 wt% brucite, and 0.71 wt% magnetite (Table 4), which equates to a 14.3% reaction of the reactant olivine. These results indicate that a comparable amount of olivine reacted in both experiments. There was no weight loss evident in the TGA results for either experiment that could be attributed to TVG minerals, probably because of their low abundance or because the dehydroxylation temperature for these minerals might overlap with that of brucite. Hence, the calculated abundance of brucite from TGA could be slightly overestimated.

Mössbauer spectroscopy (MB) was performed on the reacted solids to place additional constraints on the Fe-bearing phases. Prior to MB analysis, the solids were treated to remove some of the olivine and magnetite to reduce the signal from these components to focus on other secondary products, particularly chrysotile. The treatment involved sonicating a portion of the bulk sample with ethanol in a glass vial, and pipetting off the fine-grained suspended fraction for the MB analysis (see Online Materials¹). During this process, magnetite was removed by placing a strong magnet next to the vial while pipetting off the ethanol. Despite this treatment, a substantial amount of olivine remained in the treated solids.

TABLE 4. Results of thermogravimetric analyses for the experiments

	SO4red300	SO4red328
TGA weight loss (%):		
Serpentine	1.64	1.88
Brucite	0.22	0.24
Secondary minerals (wt%):		
Serpentine	12.8	14.6
Brucite	0.71	0.79
Magnetite ^a	0.68	0.71
Total reaction (%) ^b	12.6	14.3

^a From magnetization measurements.

^b Estimated percent of original olivine reacted, by mass. See Online Materials¹ for methods.

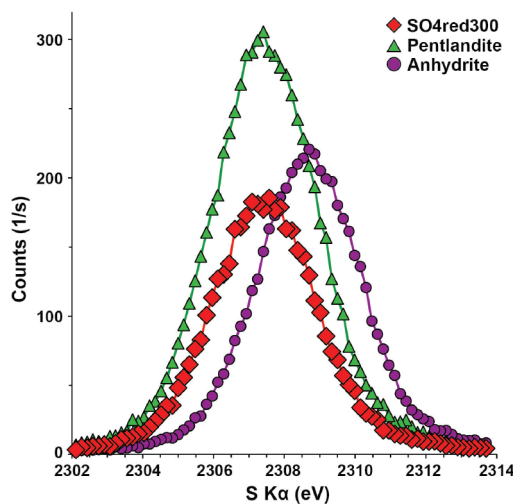


FIGURE 6. Wavelength-dispersive X-ray spectroscopy scan for the mineral identified as haapalaite from SO4red300 compared with those for Astimex standards pentlandite and anhydrite. (Color online.)

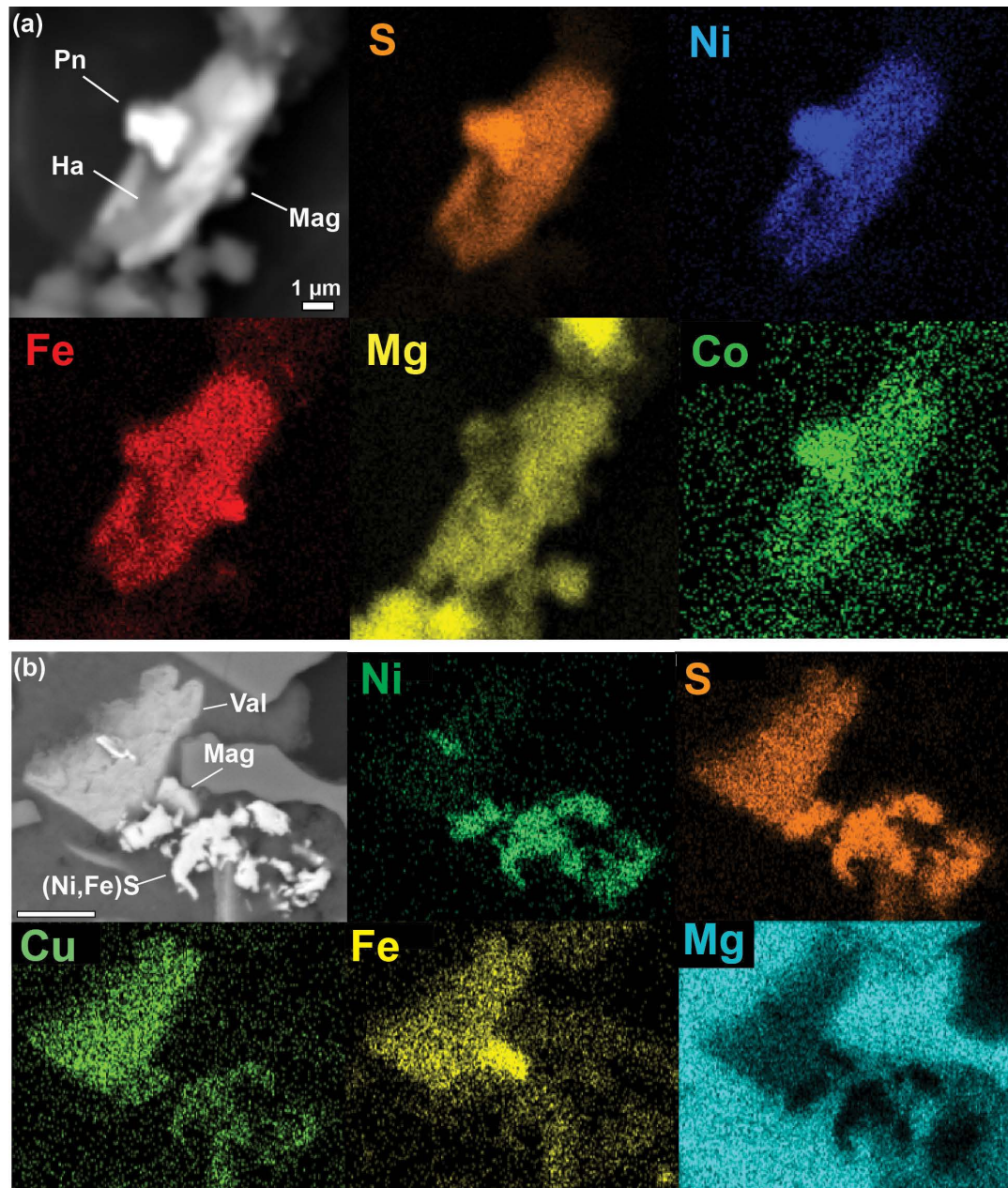


FIGURE 7. Element distribution maps obtained using EDS. (a) Haapalaite (Ha) from SO4red300 with associated pentlandite (Pn) and magnetite (Mag). Note enrichments in Ni and Co in the pentlandite relative to the haapalaite. (b) Vallerite (Val) from SO4red328 with associated Ni,Fe sulfide and magnetite. These minerals are embedded in a mat of chrysotile fibers along with relict olivine. Scale bar in b is 5 μ m. (Color online.)

The resulting MB spectra for both experiments were fit with three doublets, two assigned to Fe^{II} and one to Fe^{III} (Table 5; Online Materials¹ Figs. S10 and S11). The Fe^{II} doublets with quadrupole shift (QS) \approx 3.1 and isomer shift (IS) \approx 1.14 are assigned to olivine, and the other Fe^{II} doublets with QS \approx 2.9 and IS \approx 1.13 are assigned to chrysotile. However, because the hyperfine parameters for olivine and chrysotile are very similar to one another (Online Materials¹ Figs. S10 and S11) and the chrysotile from the experiments has very low Fe contents, there may be some overlap in the peaks assigned to these minerals and the resulting estimates for relative areas assigned to each mineral have relatively high uncertainties (Table 5).

The parameters for the Fe^{III} doublet are similar to tetrahedral site in serpentine, although there may be some contribution from the octahedral site as well (Online Materials¹ Fig. S11). There were no doublets observed for brucite or TVG minerals, which likely reflects the low abundances of these components as well as the low Fe content of brucite.

DISCUSSION

Pathway for TVG mineral formation

To our knowledge, this is the first instance where members of the tochilinite-vallerite group have been reported as reaction

TABLE 5. Room-temperature hyperfine magnetic Mössbauer parameters for the treated experiment samples

Sample	QS (mm/s)	IS (mm/s)	% ^a	Assignment
SO4red300	3.07	1.14	49	Fe ^{II} (Ol)
	2.88	1.13	47	Fe ^{II} (Ctl)
	0.39	0.31	4	Fe ^{III} (Ctl)
SO4red328	3.10	1.15	34	Fe ^{II} (Ol)
	2.90	1.13	63	Fe ^{II} (Ctl)
	0.49	0.27	3	Fe ^{III} (Ctl)
SC olivine ^b	3.00	1.18	100	Fe ^{II}

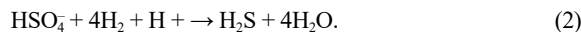
Notes: Ol = olivine; Ctl = chrysotile.

^a Relative abundances of components.

^b Data for SC olivine from McCollom et al. (2016).

products during laboratory simulation of serpentinization. It seems likely, however, that minerals from this group have formed in other sulfur-bearing serpentinization experiments conducted under comparable conditions, but that they went unrecognized owing to their sparse distribution and morphological similarity to brucite. In this respect, the high contrast of the metal-rich TVG minerals when examined by SEM in backscattered electron mode was crucial in their identification (Fig. 4), and the use of similar methods to inspect the solids from future laboratory serpentinization studies may reveal a more common occurrence.

The TVG minerals and the accompanying sulfides likely precipitated through reaction of dissolved H₂S with cations supplied primarily from dissolution of olivine. Reduction of sulfate made a significant contribution to the H₂S that precipitated in these minerals, as indicated by: (1) the relatively low amount of H₂ accumulated in the experiments compared with the amounts generated in sulfate-free experiments conducted at the same conditions (Fig. 1); (2) the increasing concentration of ΣH₂S as the experiments proceeded; and (3) the incorporation of the ³⁴S label from dissolved sulfate into reduced S in the solids and into ΣH₂S (Fig. 2). These observations are consistent with sulfate reduction according to the reaction:



The dissolved H₂S then combined with cations derived from the dissolution of the reactant minerals (Fe, Ni, Cu, and Mg) to precipitate the TVG and sulfide minerals.

Additional evidence that sulfate reduction contributed to the formation of secondary minerals comes from Ni mass balance. The Ni present in the TVG minerals and in Ni,Fe-sulfides most likely came from dissolution of olivine since there are no other identified sources of Ni in the experiments. Based on the amount of olivine initially included in SO4red300 (14 g), the extent of reaction (12.8%), and the Ni content of olivine (0.38 wt% NiO), the amount of Ni released from the reactants was ~91 μmoles. For a Ni:S ratio of one, the Ni alone would have exceeded the amount of S originally added to the experiment as FeS (77 μmoles), so the addition of reduced S from sulfate reduction was required to account for the secondary minerals. For SO4red328, the dissolution of olivine released ~103 μmoles Ni. Given the absence of added FeS for this experiment, even greater amounts of sulfate reduction are required to explain the precipitation of secondary minerals.

It is somewhat more problematic to determine the source of Cu for the formation of vallerite in SO4red328. Although trace amounts of Cu-bearing minerals were found as contaminants during inspection of the reactant by SEM (Online Materials¹ Fig. S2), it is not certain that these were present in sufficient amounts to

account for the vallerite. Other possible sources include nanoscale Cu minerals that went undetected during inspection of the reactant olivine or trace amounts of Cu present in the olivine itself, either within the mineral matrix or as very small inclusions. Because the thread lubricant (Jet-Lube SS-30) used in preparation of the reaction cell contains native Cu, it also is possible that the experiment was somehow contaminated with lubricant during set-up and that this contributed to the precipitation of vallerite. Prior to the experiments, lubricant is applied to the threads of the titanium closure piece of the reaction cell (Online Materials¹ Fig. S1), and conceivably, some of this lubricant could have gotten into the cell itself. However, because the lubricant was carefully applied to the threads with a cotton swab and the threads are external to the sealing surface of the reaction cell, it is unlikely that any significant contamination could have occurred. In addition, the interior of the reaction cell is cleaned with 6 N HCl between experiments, so carryover from a previous experiment is unlikely.

At this time, it is unclear why vallerite precipitated as the TVG mineral in SO4red328 while haapalaite precipitated in SO4red300. One possibility, however, is that the higher temperature and lack of added pyrrhotite in SO4red328 favored greater partitioning of Ni from olivine into secondary sulfide minerals, as reflected by the higher Ni:(Ni+Fe) ratio in the sulfides present in SO4red328 than in SO4red300 (Table 1). This may have resulted in less Ni being available to partition into TVG minerals, leading to precipitation of vallerite rather than haapalaite. Alternatively, the difference could reflect variation in the thermodynamic stability of TVG minerals as a function of temperature and activities of H₂ and H₂S. Other explanations are also possible, and additional experimental work will be needed to better understand what factors control the composition of TVG minerals during serpentinization.

Potential pathways for TVG mineral formation in serpentinites

There have been numerous reports of TVG minerals in natural serpentinites suggesting that their occurrence is widespread, although they are typically present in only small amounts (Jambor 1969; Clark 1970; Organova et al. 1971; Harris and Vaughan 1972; Huhma et al. 1973; van de Vusse and Powell 1983; Matsubara and Kato 1992; Alt and Shanks 1998; Beard 2000; Beard and Hopkinson 2000; Dietze and Kontny 2011; Boschi et al. 2017). Tochilinite and vallerite are the most commonly reported TVG minerals in serpentinite, but haapalaite has been reported in a few localities (Huhma et al. 1973; Matsubara and Kato 1992; Beard 2000). The chemistry of this mineral group has received little study and, consequently, the potential for solid-solution mixing and the compositional boundaries between end-members are poorly defined. Nevertheless, from the data currently available for natural samples and the experimental results, it is evident that considerable solid solution mixing is possible within this mineral group, particularly with respect to Fe, Ni, Cu, and Mg contents (e.g., Beard 2000; Mikhlin et al. 2022a).

Despite their low abundance, TVG minerals have the potential to supply useful information about the local chemical and physical environment at the time they precipitated. At present, however, the conditions leading to precipitation of TVG minerals in serpentinite are poorly constrained. Based on setting and mineralogical associations, some studies have inferred that conditions for the formation

of TVG minerals include low temperatures, relatively oxidizing conditions, and alkaline pH (e.g., Chamberlain and Delabio 1965; Boschi et al. 2017). In many cases, TVG minerals in serpentinites are found in close proximity to sulfide minerals, leading other authors to suggest that the TVG minerals formed through replacement of primary sulfides (Harris and Vaughan 1972; van de Vusse and Powell 1983; Zolensky and MacKinnon 1986; Matsubara and Kato 1992; Beard 2000). In still other studies, the TVG minerals are found in association with secondary magnetite, where they have sometimes been interpreted to be replacing the magnetite under relatively oxidizing conditions (Chamberlain and Delabio 1965; Matsubara and Kato 1992); however, other authors have interpreted the associated magnetite to form after TVG mineral precipitation as a consequence of a transition to more oxidizing conditions (van de Vusse and Powell 1983). In contrast to serpentinites, the Fe-rich tochilinite found in meteorites is generally thought to form through alteration of Fe-Ni alloys under highly reducing conditions at relatively low temperatures (<100 °C) and neutral-to-alkaline pH (e.g., Zolensky et al. 1993; Peng and Jing 2014; Pignatelli et al. 2017; Vacher et al. 2019).

The results of the present experiments demonstrate that TVG minerals can precipitate during serpentinization of olivine-rich ultramafic rocks at elevated temperatures, circumneutral pH, and strongly reducing conditions, potentially expanding consideration of the range of conditions under which these minerals form in natural serpentinites. In addition, there is no indication that the haapalaite and vallerite formed as an alteration product of preexisting sulfides or magnetite, as inferred for some occurrences of TVG minerals in serpentinite. Although pyrrhotite was initially present in the SO4red300 experiment, it is unlikely that direct replacement of this mineral was involved in haapalaite formation since (1) the haapalaite was never observed spatially associated with pyrrhotite, and (2) alteration of pyrrhotite would not account for the elevated Ni and Co contents of the haapalaite. Furthermore, there was no pyrrhotite included in the reactants for SO4red328, so it could not have been a precursor to vallerite. Instead, the association of TVG minerals with sulfides and magnetite in our experiments (Figs. 4 and 7) appears to result from concurrent precipitation of these secondary phases rather than from replacement. This observation raises the possibility that, in some instances, the association of TVG minerals with sulfides and magnetite in natural samples might arise from simultaneous precipitation as serpentinization progressed rather than as a replacement for preexisting sulfides or oxides.

The results also suggest a possible alternative pathway for TVG mineral formation during serpentinization that involves the reduction of seawater-derived sulfate. In seafloor hydrothermal systems, much of the sulfate in seawater is removed from circulating fluids through precipitation of anhydrite or other sulfate minerals as the temperature of the fluid increases (Bischoff and Seyfried 1978). Nevertheless, some sulfate may persist in the fluids as they circulate through the hydrothermal system (just as some dissolved sulfate persisted throughout the experiments; Fig. 1), and this sulfate could undergo reduction to H₂S when the fluids penetrate into actively serpentinizing rocks at elevated temperatures. Indeed, there is isotopic evidence that reduction of seawater sulfate has occurred in some seafloor serpentinites (e.g., Alt and Shanks 1998), although it is possible that this is biotic rather than abiotic. The resulting H₂S may then react with dissolved Fe, Mg, Ni, and Cu released

from olivine, pyroxene, or other minerals to form TVG minerals.

Based on the experimental results, such processes could potentially occur at elevated temperatures, at least as high as 328 °C and at circumneutral to mildly acidic conditions. Similar reactions might be possible at lower temperatures and alkaline pH; however, the rate of sulfate reduction may be much slower under these circumstances, so this possibility needs to be investigated experimentally. In any event, it appears plausible that the TVG minerals observed in some natural serpentinites may have precipitated as the rocks were actively undergoing serpentinization, with the reduction of seawater sulfate contributing to the reduced S. Analysis of the sulfur isotopic composition of minerals from this group in future studies of natural samples would allow this possibility to be tested.

IMPLICATIONS

Although tochilinite-vallerite group minerals are relatively sparse components of serpentinites, they have the potential to provide useful constraints on the environmental conditions present when they formed (fluid composition, sulfur source, temperature, etc.). In turn, this information may provide new insights into processes and reaction pathways during the serpentinization of ultramafic rocks. As the first report of minerals from this group to be identified in a laboratory serpentinization experiment, the results provide initial constraints on conditions for their formation that can be expanded upon in future studies.

ACKNOWLEDGMENTS AND FUNDING

We thank Eric Ellison for assistance with obtaining Raman spectra. This research was supported by the NASA Habitable Worlds program through award numbers NNN17ZDA001N-HW, 80NSSC19K0705, and 80NSSC19K0600. The IRM is a U.S. National Multi-user Facility supported through the Instrumentation and Facilities program of the National Science Foundation, Earth Sciences Division (EAR-2153786), and by funding from the University of Minnesota. This is IRM contribution no. 2101.

REFERENCES CITED

- Alt, J.C. and Shanks, W.C. III (1998) Sulfur in serpentinized oceanic peridotites: Serpentinization processes and microbial sulfate reduction. *Journal of Geophysical Research*, 103 (B5), 9917–9929, <https://doi.org/10.1029/98JB00576>.
- Beard, J.S. (2000) Occurrence and composition of tochilinite and related minerals in Site 1068 serpentinites. In M.-O. Beslier, R.B. Whitmarsh, P.J. Wallace, and J. Girardeau, Eds., *Proceedings of the Ocean Drilling Program Scientific Results*, 173, 1–9.
- Beard, J.S. and Hopkinson, L. (2000) A fossil, serpentinization-related hydrothermal vent, Ocean Drilling Program, Leg 173, Site 1068 (Iberia Abyssal Plain): Some aspects of mineral and fluid chemistry. *Journal of Geophysical Research*, 105 (B7), 16,527–16,539, <https://doi.org/10.1029/2000JB900073>.
- Bischoff, L. and Seyfried, W.E. Jr. (1978) Hydrothermal chemistry of seawater from 25 degrees to 350 degrees C. *American Journal of Science*, 278, 838–860, <https://doi.org/10.2475/ajs.278.6.838>.
- Blaauw, C., Stroink, G., Leiper, W., and Zentilli, M. (1979) Crystal-field properties of Fe in brucite Mg(OH)₂. *Physica status solidi (b)*, 92, 639–643.
- Boschi, C., Dini, A., Baneschi, I., Bedini, F., Perchiazzoli, N., and Cavallo, A. (2017) Brucite-driven CO₂ uptake in serpentinized dunites (Ligurian Ophiolites, Montecastelli, Tuscany). *Lithos*, 288–289, 264–281, <https://doi.org/10.1016/j.lithos.2017.07.005>.
- Carroll, M.R. and Rutherford, M.J. (1988) Sulfur speciation in hydrous experimental glasses of varying oxidation state: Results from measured wavelength shifts of sulfur X-rays. *American Mineralogist*, 73, 845–849.
- Chamberlain, J.A. and Delabio, R.N. (1965) Mackinawite and vallerite in the Muskox Intrusion. *American Mineralogist*, 50, 682–695.
- Clark, A.H. (1970) A probable second occurrence of Jambor's "fibrous iron sulfide". *American Mineralogist*, 55, 283–284.
- Coplen, T.B., Hopple, J.A., Böhlke, J.K., Peiser, H.S., Rieder, S.E., Krouse, H.R., Rosman, K.J.R., Ding, T., Vocke, R.D.J., Révész, K.M., Lamberty, A., Taylor, P., and DeBièvre, P. (2002) Compilation of Minimum and Maximum Isotope Ratios of Selected Elements in Naturally Occurring Terrestrial Materials and Reagents, United States Geological Survey, pp. 98.
- Dietze, F. and Kontny, A. (2011) A study of rock magnetic properties of serpentinites from the Outokumpu Deep Drill Hole, Finland. *Geological Survey of Finland Special Paper*, 51, 133–150.

Evans, H.T. Jr. and Allmann, R. (1968) The crystal structure and crystal chemistry of valleriite. *Zeitschrift für Kristallographie*, 127, 73–93, <https://doi.org/10.1524/zkri.1968.127.1.4.73>.

Gubaidelina, T.V., Chistyakova, N.I., and Rusakov, V.S. (2007) Mössbauer study of layered iron hydroxides: Tochilinite and valleriite. *Bulletin of the Russian Academy of Science*, 71, 1269–1272.

Harris, D.C. and Vaughan, D.J. (1972) Two fibrous iron sulfides and valleriite from Cyprus with new data on valleriite. *American Mineralogist*, 57, 1037–1052.

Harris, D.C., Cabri, L.J., and Stewart, J.M. (1970) A “vallerite-type” mineral from Noril’sk, Western Siberia. *American Mineralogist*, 55, 2110–2114.

Houghton, J., Scarponi, D., Capraro, L., and Fike, D.A. (2022) Impact of sedimentation, climate and sea level on marine sedimentary pyrite sulfur isotypes: Insights from the Valle di Manche section (Lower-Middle Pleistocene, southern Italy). *Palaeogeography, Palaeoclimatology, Palaeoecology*, 585, 110730, <https://doi.org/10.1016/j.palaeo.2021.110730>.

Huhma, M., Vuorelainen, Y., Häkli, T.A., and Papunen, H. (1973) Haapalaite, a new nickel–iron sulphide of the valleriite type from east Finland. *Bulletin of the Geological Society of Finland*, 45, 103–106, <https://doi.org/10.17741/bgsf/45.2.001>.

Jackson, M. and Solheid, P. (2010) On the quantitative analysis and evaluation of magnetic hysteresis data. *Geochemistry, Geophysics, Geosystems*, 11, Q04Z15, <https://doi.org/10.1029/2009GC002932>.

Jambor, J.L. (1969) Coalignite from the Muskox intrusion, Northwest Territories. *American Mineralogist*, 54, 437–447.

Janecky, D.R. and Seyfried, W.E. Jr. (1986) Hydrothermal serpentinization of peridotite within the oceanic crust: Experimental investigations of mineralogy and major element chemistry. *Geochimica et Cosmochimica Acta*, 50, 1357–1378, [https://doi.org/10.1016/0016-7037\(86\)90311-X](https://doi.org/10.1016/0016-7037(86)90311-X).

Klein, F. and Bach, W. (2009) Fe–Ni–Co–O–S phase relations in peridotite–seawater interactions. *Journal of Petrology*, 50, 37–59, <https://doi.org/10.1093/petrology/egn071>.

Klein, F., Humphris, S.E., and Bach, W. (2020) Brucite formation and dissolution in oceanic serpentinite. *Geochemical Perspectives Letters*, 16, 1–5, <https://doi.org/10.7185/geochemlet.2035>.

Makovicky, E. and Hyde, B.G. (1981) Non-commensurate (misfit) layer structures. Conference proceedings, Inorganic Chemistry, Structure and Bonding, vol. 46, p. 101–170. Springer.

Mann, J.L., Vocke, R.D. Jr., and Kelly, W.R. (2009) Revised $\delta^{34}\text{S}$ reference values for IAEA Sulfur Isotope Reference Materials S-2 and S-3. *Rapid Communications in Mass Spectrometry*, 23, 1116–1124.

Matsubara, S. and Kato, A. (1992) Tochilinite in ultrabasic rock from Kurotani, Gifu Prefecture, Central Japan. *Bulletin of the National Science Museum of Tokyo*, Series C, 18, 117–120.

McCollom, T.M. and Bach, W. (2009) Thermodynamic constraints on hydrogen generation during serpentinization of ultramafic rocks. *Geochimica et Cosmochimica Acta*, 73, 856–875, <https://doi.org/10.1016/j.gca.2008.10.032>.

McCollom, T.M. and Seewald, J.S. (2001) A reassessment of the potential for reduction of dissolved CO_2 to hydrocarbons during serpentinization of olivine. *Geochimica et Cosmochimica Acta*, 65, 3769–3778.

McCollom, T.M., Seewald, J.S., and Simoneit, B.R.T. (2001) Reactivity of monocyclic aromatic compounds under hydrothermal conditions. *Geochimica et Cosmochimica Acta*, 65, 455–468.

McCollom, T.M., Klein, F., Robbins, M., Moskowitz, B., Berqué, T.S., Bach, W., and Templeton, A. (2016) Temperature trends for reaction rates, hydrogen generation, and partitioning of iron during experimental serpentinization of olivine. *Geochimica et Cosmochimica Acta*, 181, 175–200, <https://doi.org/10.1016/j.gca.2016.03.002>.

McCollom, T.M., Klein, F., Moskowitz, B., Berqué, T.S., Bach, W., and Templeton, A. (2020) Hydrogen generation and iron partitioning during experimental serpentinization of an olivine–pyroxene mixture. *Geochimica et Cosmochimica Acta*, 282, 55–75, <https://doi.org/10.1016/j.gca.2020.05.016>.

Mikhlin, Y., Borisov, R.V., Vorobev, S.A., Tomashevich, Y.V., Romanchenko, A.S., Likhatski, M.N., Karacharov, A.A., Bayukov, O.A., Knyazev, Y.V., Velikanov, D.A., and others. (2022a) Synthesis and characterization of nanoscale composite particles formed by 2D layers of Cu–Fe sulfide and Mg-based hydroxide. *Journal of Materials Chemistry A, Materials for Energy and Sustainability*, 10, 9621–9634, <https://doi.org/10.1039/D2TA00877G>.

Mikhlin, Y., Likhatski, M., Romanchenko, A., Vorobev, S., Tomashevich, Y., Fetisova, O., Bayukov, O., Knyazev, Y., Nemtsev, I., Karasev, S., Karacharov, A., and Borisov, R. (2022b) Vallerite-containing ore from Kingash deposit (Siberia, Russia): Mössbauer and X-ray photoelectron spectroscopy characterization, thermal and interfacial properties. *Journal of Siberian Federal University Chemistry*, 15, 303–317.

Mücke, A. (2017) Review on mackinawite and valleriite: Formulae, localities, associations and intergrowths of the minerals, mode of formation and optical features in reflected light. *Journal of Earth Science & Climatic Change*, 8, 11, <https://doi.org/10.4172/2157-7617.1000419>.

O’Hanley, D.S. and Dyar, M.D. (1993) The composition of lizardite 17 and the formation of magnetites in serpentinites. *American Mineralogist*, 78, 391–404.

——— (1998) The composition of chrysotile and its relationship with lizardite. *Canadian Mineralogist*, 36, 727–739.

Organova, N.I., Genkin, A.D., Drits, V.A., Dmitrik, A.L., and Kuzmina, O.V. (1971) Tochilinit–novyi–sulfide–gidrookisel zheleza I magniya (Tochilinite: A new sulfide hydroxide of iron and magnesium). *Zapiski Vsesoyuznogo Mineralogicheskogo Obschestva*, 4, 477–487 (in Russian).

Organova, N.I., Drits, V.A., and Dmitrik, A.L. (1973) Structural study of tochilinite. Part 1. The isometric variety. *Soviet Physics, Crystallography*, 17, 667–671.

——— (1974) Structural study of tochilinite. II. Acicular variety: Unusual diffraction patterns. *Soviet Physics, Crystallography*, 18, 606–609.

Palmer, E.E. and Lauretta, D.S. (2011) Aqueous alteration of kamacite in CM chondrites. *Meteoritics & Planetary Science*, 46, 1587–1607, <https://doi.org/10.1111/j.1945-5100.2011.01251.x>.

Peng, Y. and Jing, Y. (2014) Hydrothermal preparation of analogous matrix minerals of CM carbonaceous chondrites from metal alloy particles. *Earth and Planetary Science Letters*, 408, 252–262, <https://doi.org/10.1016/j.epsl.2014.10.020>.

Peng, Y., Xu, L., Xi, G., Zhong, C., Lu, J., Meng, Z., Li, G., Zhang, S., Zhang, G., and Qian, Y. (2007) An experimental study on the hydrothermal preparation of tochilinite nanotubes and tochilinite–serpentine–intergrowth nanotubes from metal particles. *Geochimica et Cosmochimica Acta*, 71, 2858–2875, <https://doi.org/10.1016/j.gca.2007.03.012>.

Petruck, W., Harris, D.C., and Murray, E.J. (1971) An occurrence of valleriite from New Imperial Mine, Yukon. *Canadian Mineralogist*, 10, 885–888.

Pignatelli, I., Marrocchi, Y., Mugnaioli, E., Bourdelle, F., and Gounelle, M. (2017) Mineralogical, crystallographic and redox features of the earliest stages of fluid alteration in CM chondrites. *Geochimica et Cosmochimica Acta*, 209, 106–122, <https://doi.org/10.1016/j.gca.2017.04.017>.

Robinson, B.W. (1995) Sulphur isotope standards. Reference and intercomparison materials for stable isotopes of light elements. International Atomic Energy Agency, Vienna, Austria. IAEA-TECDOC-825, 39–45.

Seyfried, W.E. Jr., Janecky, D.R., and Berndt, M.E. (1987) Rocking autoclaves for hydrothermal experiments, II. The flexible reaction-cell system. In G.C. Ulmer and H.L. Barnes, Eds., *Hydrothermal Experimental Techniques*, p. 216–239. Wiley.

Springer, A. (1968) Electron microprobe analyses of mackinawite and valleriite. *Neues Jahrbuch für Mineralogie, Monatshefte*, 8, 252–258.

Toland, W.G. (1960) Oxidation of organic compounds with aqueous sulfate. *Journal of the American Chemical Society*, 82, 1911–1916, <https://doi.org/10.1021/ja01493a020>.

Vacher, L.G., Marrocchi, Y., Villeneuve, J., Verdier-Paoletti, M.J., and Gounelle, M. (2017) Petrography and C & O isotopic characteristics of the earliest stages of aqueous alteration of CM chondrites. *Geochimica et Cosmochimica Acta*, 213, 271–290, <https://doi.org/10.1016/j.gca.2017.06.049>.

Vacher, L.G., Truche, L., Faure, F., Tissandier, L., Mosser-Ruck, R., and Marrocchi, Y. (2019) Deciphering the conditions of tochilinite and cronstedtite formation in CM chondrites from low temperature hydrothermal experiments. *Meteoritics & Planetary Science*, 54, 1870–1889, <https://doi.org/10.1111/maps.13317>.

van de Vusse, R. and Powell, R. (1983) The interpretation of pyrotite–pentlandite–tochilinite–magnetite–magnesite textures in serpentinites from Mount Keith, Western Australia. *Mineralogical Magazine*, 47, 501–505, <https://doi.org/10.1180/minmag.1983.047.345.11>.

Viti, C. (2010) Serpentine minerals discrimination by thermal analysis. *American Mineralogist*, 95, 631–638.

Wallace, P.J. and Carmichael, I.S.E. (1994) S speciation in submarine basaltic glasses as determined by measurements of SKa X-ray wavelength shifts. *American Mineralogist*, 79, 161–167.

Wolery, T.J. and Jarek, R.L. (2003) Software user’s manual: EQ3/6, ver. 8.0. Lawrence Livermore National Laboratory.

Zhang, T., Amrani, A., Ellis, G.S., Ma, Q., and Tang, Y. (2008) Experimental investigation on thermochemical sulfate reduction by H_2S initiation. *Geochimica et Cosmochimica Acta*, 72, 3518–3530, <https://doi.org/10.1016/j.gca.2008.04.036>.

Zolensky, M. (1987) Tochilinite in C2 carbonaceous chondrites: A review with suggestions. *Lunar and Planetary Science Conference*, XVIII, 1132–1133 (abstract).

Zolensky, M. and MacKinnon, I.D.R. (1986) Microstructures of cylindrical tochilinites. *American Mineralogist*, 71, 1201–1209.

Zolensky, M., Barrett, R., and Browning, L. (1993) Mineralogy and composition of matrix and chondrule rims in carbonaceous chondrites. *Geochimica et Cosmochimica Acta*, 57, 3123–3148, [https://doi.org/10.1016/0016-7037\(93\)90298-B](https://doi.org/10.1016/0016-7037(93)90298-B).

MANUSCRIPT RECEIVED JUNE 4, 2022

MANUSCRIPT ACCEPTED JANUARY 4, 2023

ACCEPTED MANUSCRIPT ONLINE JANUARY 19, 2023

MANUSCRIPT HANDLED BY DANIEL GREGORY

Endnote:

¹Deposit item AM-24-18625. Online Materials are free to all readers. Go online, via the table of contents or article view, and find the tab or link for supplemental materials.